Research article

Guorui Zhang, Ying Gu, Qihuang Gong and Jianjun Chen*

Symmetry-tailored patterns and polarizations of single-photon emission

https://doi.org/10.1515/nanoph-2020-0208
Received March 25, 2020; accepted June 11, 2020; published online July 8, 2020

Abstract: Due to small optical mode volumes and linear polarizations of surface-plasmon-polariton (SPP) resonant modes in metallic antennas, it is very difficult to obtain complex emission patterns and polarizations for single-photon emitters. Herein, nonresonant enhancement in a silver nanowire is used to both enhance emission rates and extract a *z*-oriented dipole, and then the symmetry of metallic nanostructures is proposed to tailor the patterns and polarizations of single-photon emission. The emission pattern of a quantum dot located close to a metallic nanostructure with a symmetric axis is split into multiple flaps. The number of splitting flaps is equal to the order of the symmetric axis. Moreover, the electric vectors of the emitted photons become centrally symmetric about the symmetric axis. The above phenomena are well explained by both a simulation and an image dipole model. The structural-symmetry-tailoring mechanism may open up a new avenue in the design of multifunctional and novel quantum-plasmonic devices.

Keywords: image dipole model; metallic nanostructures; pattern tailoring; polarization tailoring; single-photon emitters; structural symmetry.

***Corresponding author: Jianjun Chen**, Department of Physics and Applied Optics Beijing Area Major Laboratory, Beijing Normal University, Beijing 100875, China; State Key Laboratory for Mesoscopic Physics, School of Physics, Peking University, Beijing, 100871, China; Frontiers Science Center for Nano-optoelectronics & Collaborative Innovation Center of Quantum Matter, Peking University, Beijing, 100871, China; Collaborative Innovation Center of Extreme Optics, Shanxi University, Taiyuan, Shanxi, 030006, China; and Peking University Yangtze Delta Institute of Optoelectronics, Nantong 226010, Jiangsu, China, E-mail: jjchern@pku.edu.cn. https://orcid.org/0000-0002-1050-1189
Guorui Zhang: State Key Laboratory for Mesoscopic Physics, School of Physics, Peking University, Beijing, 100871, China
Ying Gu and Qihuang Gong: State Key Laboratory for Mesoscopic Physics, School of Physics, Peking University, Beijing, 100871, China; Frontiers Science Center for Nano-optoelectronics & Collaborative Innovation Center of Quantum Matter, Peking University, Beijing, 100871, China; and Collaborative Innovation Center of Extreme Optics, Shanxi University, Taiyuan, Shanxi, 030006, China

1 Introduction

Single-photon emitters are of great importance for applications in quantum technologies such as quantum computing, quantum simulation, quantum walk, quantum memory, and precision measurement [1]. Quantum dots, [2, 3] nitrogen-vacancy (NV) centers, [4] and transition metal dichalcogenides (TMDCs) [5–7] are widely used to realize single-photon emitters. These quantum emitters have a degenerate transition dipole oriented isotropically along two orthogonal axes. Commonly, the photons emitted from these nanoscale quantum emitters have omni-directional emission, poor polarization, and onefold Airy pattern [1–7] in the far field. These properties considerably hamper practical implementation of these quantum emitters, such as collection efficiency, mode matching, and multifunctionality.

To address these problems, enormous efforts have been made to design various metallic antennas to manipulate the photons emitted from quantum emitters. These metallic antennas support surface-plasmon-polariton (SPP) resonant modes with strong field enhancements, small optical mode volumes, and linear polarizations (electric vectors mainly perpendicular to the metal surface) [8–18]. When a quantum emitter is located very close to a metallic antenna (several nanometers), the photons emitted from the quantum emitter are mainly coupled to the strong SPP resonant modes rather than directly radiating to free space [19]. Therefore, the far-field properties of the photons emitted from the hybrid system (consisting of the quantum emitter and the metallic antenna) are principally determined by SPP resonant modes. As a result, the emission rate, [9–14, 20] emission direction, [15–18] and emission polarization [8] can be efficiently manipulated by SPP resonant modes.

For example, by locating a single quantum emitter close to silver nanoparticles (placed on a metal surface), [9–11, 13, 14] Bullseye antennas, [12] and gold nanorods, [20] the emission rates of the quantum emitter were greatly increased because of the Purcell enhancement [14]. The increased emission rates of quantum emitters greatly brighten single-photon emitters, which is important for quantum key

distribution, cluster-state quantum computing, and the use of Bell-state sources for memory-based repeaters [1, 21]. By designing a variety of metallic antennas, including optical patch antennas, [8–11] bullseye antennas, [12, 16] parabolic antennas, [17] and Yagi–Uda antennas, [18] a large directivity of the photons emitted from quantum emitters was obtained when quantum emitters were properly placed in relation to these metallic antennas. The large directivity considerably increased the collection efficiency of the photons emitted from quantum emitters.

It should be noted that emission wavelengths of quantum emitters should match resonant wavelengths of metallic antennas in these hybrid systems [8–18] due to the use of the strong SPP resonant effect in metallic antennas. The far-field emission patterns of quantum emitters are a onefold Airy pattern in the far field owing to nanoscale SPP resonant modes (optical mode volume $V << \lambda^3$) in metallic antennas, and more complex patterns cannot be realized. Moreover, photons emitted from quantum emitters in these hybrid systems [8–18] are linearly polarized because of linear polarizations of nanoscale SPP resonant modes (e.g., dipole resonance) in metallic antennas, and other polarization states of single-photon emission are difficult to achieve. Both of the above issues greatly limit applications of single-photon emitters in the areas of multiple-degree-of-freedom quantum memory, quantum correlation, quantum lithography, quantum imaging, quantum encoding, and quantum processing [22–28].

In this letter, we propose to use symmetry of a metallic nanostructure rather than SPP resonant modes to tailor emission patterns and polarizations of a single-photon emitter. When a single quantum dot is located close to a metallic nanostructure with a symmetric axis (corresponding to a symmetry group), it is found that the emission pattern of the quantum dot is split into multiple flaps. The number of splitting flaps is equal to the order of the symmetric axis. Moreover, the electric vectors of the emitted photons become centrally symmetric about the symmetric axis of the metallic nanostructure, revealing a radial polarization state. Since there is no resonant effect in the hybrid system, matching of the emission wavelength of the quantum dot and the resonant wavelength of the metallic nanostructure is no longer required. To understand the underlying mechanism of these pattern- and polarization-tailoring phenomena in the hybrid system, both a simulation and an image dipole model are provided. The tailoring of the emission patterns and polarizations of the single quantum dot by the structural symmetry might provide more degrees of freedom and more functionalities in quantum devices [22–28].

2 Results

2.1 Experiments

Herein, the basic unit of the metallic nanostructure comprises a silver nanowire placed on a metal substrate (gold or silver), and a quantum dot is located above the silver nanowire, as shown in Figure 1a. The cross section of the silver nanowire is a pentagon, [29] as displayed in Figure 1b. The radius of the sliver nanowire is R, and a thin poly(methyl methacrylate) (PMMA) film is used to protect the silver nanowire from oxidation. The coordinate system is also given in Figure 1a. The x-y plane lies on the surface of the gold substrate. The z-axis is perpendicular to the gold substrate and passes through the single quantum dot and the top edge of the silver nanowire. The single quantum dot is located at $(0, 0, z)$, where $z = [1+\sin(72°)]R + d$. Here, d is the distance between the quantum dot and the top edge of the silver nanowire. In this hybrid system, it is clear that the z-axis is a twofold symmetric axis, corresponding to the C_2 point group. The dark-field image of silver nanowires with radii ranging from 80 to 140 nm is displayed in Figure 1c, and the detailed fabrication can be seen in Appendix A: Fabrication. The cross section of one silver nanowire is depicted in the scanning electron microscopy image in Figure 1d, revealing a pentagon shape.

Then, the photons emitted from the quantum dots are imaged by a homemade microscope (see Appendix B: Measurement), and the results are shown in Figure 2a. The small bright white spots with the Airy pattern in Figure 2a are the quantum dots. These small bright white spots blink with time, which is the nature of a single quantum dot [2, 30, 31]. Moreover, it is also observed that some white spots are split into two distinct flaps in the optical image, as shown by the red dashed box in Figure 2a. A zoomed-in image of the splitting spot is displayed in Figure 2b, and the quantum dot is located above a silver nanowire (denoted by the green dashed line in Figure 2b). In Figure 2b, the upper left and lower right flaps are denoted Flap A and B, respectively. The emission spectra for the emission with two flaps and that from the quantum dot on a glass substrate are shown in Figure 2c and d. The two spectra nearly overlap with each other, and the central wavelength of quantum dot is $\lambda_{em} = 650$ nm.

By adding a polarizer in front of the scientific complementary metal oxide semiconductor (sCMOS) camera, the polarizations of the two flaps are measured, and the results are displayed by the black dots in Figure 2e and f. Herein, the red solid lines are the fitting curves obtained by using the equation $I = I_0\cos^2(\theta)$, where θ is the angle of the

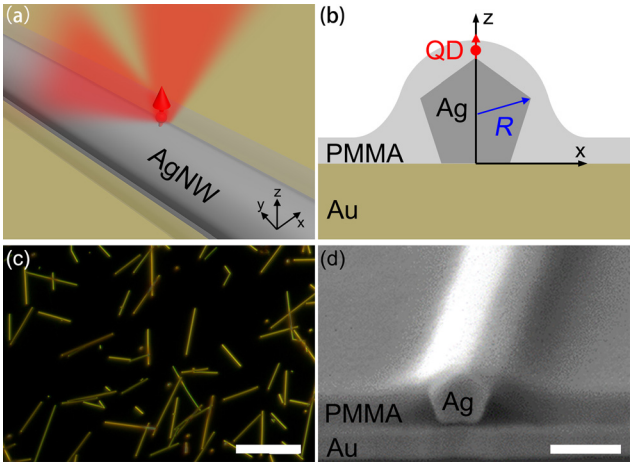

Figure 1: (a) Schematic diagram of the metallic nanostructure comprising a silver nanowire placed on a metal substrate. A quantum dot is located above the silver nanowire. (b) Cross section of the proposed structure in the *x*-*z* plane with $y = 0$ μm. The radius (R) of the sliver nanowire is defined as the distance between the center and a vertex of the pentagon. (c) Dark-field image of silver nanowires placed on a gold substrate. The scale bar is 20 μm. (d) scanning electron microscopy image of the cross section of one of the silver nanowires placed on the gold substrate. The scale bar is 200 nm.

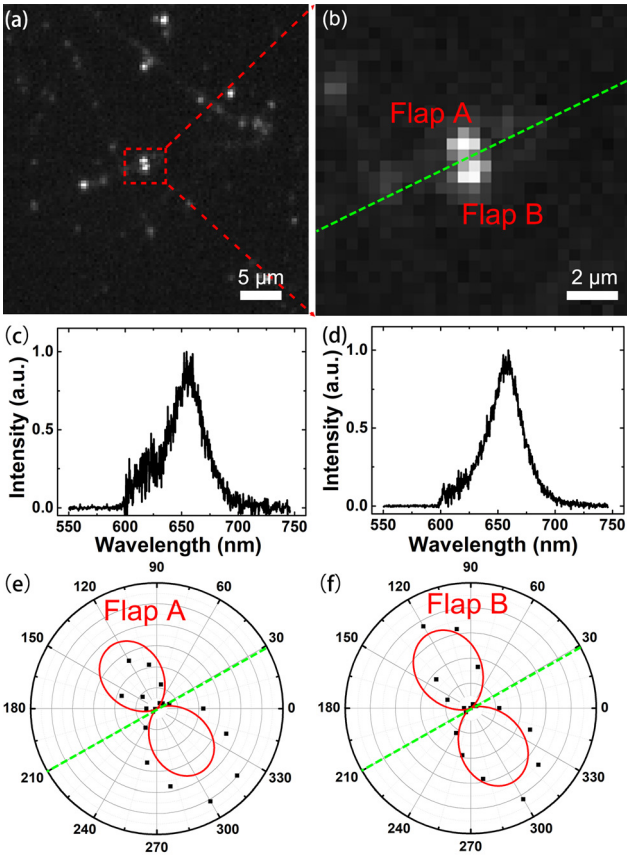

Figure 2: (a) Optical image of the collected photons emitted from the single quantum dots. The scale bar is 5 μm. (b) Zoomed-in optical image of the splitting spot. The scale bar is 2 μm. (c) Emission spectrum for the emission with two flaps. (d) Emission spectrum from the quantum dot on a glass substrate. Polar plots of the measured emission intensities of (e) Flap A and (f) Flap B as a function of the polarizer angle.

polarizer. The polarizations of the two splitting flaps (Flap A and B) are perpendicular to the silver nanowire (denoted by the green dashed lines in Figure 2e and f). The degrees of linear polarization of Flap A and Flap B are greater than 0.9. A similar splitting phenomenon was also observed for silver nanowires coated by a series of molecules [32]. In this work, the harmful effects of the splitting phenomenon from the ensemble fluorescence of molecules to super-localization techniques were deeply studied. However, pattern and polarization tailoring of the single-photon emission from a single molecule or quantum dot has not been investigated as far as we know. Pattern and polarization tailoring of the single-photon emission would provide more degrees of freedom and more functionalities in quantum communication, quantum encoding, and quantum memory [22–28].

Next, the properties of the splitting spot are investigated. First, the fluorescence intensity time traces of the two flaps (Flap A and Flap B in Figure 2b) are extracted from the video, and the results are shown in Figure 3a. A fluorescence intermittency (blinking) character and a high degree of correlation between the two flaps are observed. These observations indicate that the photons of the two flaps come from the same single quantum dot [33]. Then, the autocorrelation curve $g^2(t)$ of the photons emitted from the single quantum dot located above the silver nanowire is measured by using the Hanbury Brown and Twiss setup [19, 34]. The measurement result is shown by the blue line in Figure 3b. The data are fitted to the $g^2(t)$ formula in Ref. [19], as shown by the red line in Figure 3b. The dip in the autocorrelation curve of the collected photons is $g^2(0) \approx 0.30$ (<0.5), indicating that the single quantum dot located above the silver nanowire is a single-photon emitter.

Finally, the lifetimes of single quantum dots are measured by a time-correlated single photon counting (TCSPC) measurement system [19] (see Appendix B: Measurement), and the results are shown in Figure 3c and d. The black line in Figure 3c is the decay curve of the photons emitted from a single quantum dot doped in PMMA, which is spin-coated on a glass substrate. By fitting the black line with a double exponential function, the fast lifetime is found to be approximately $\tau^{r}_{fast} = 6.8$ ns, and the slow lifetime is approximately $\tau^{r}_{slow} = 30.3$ ns. Moreover, the lifetime of the

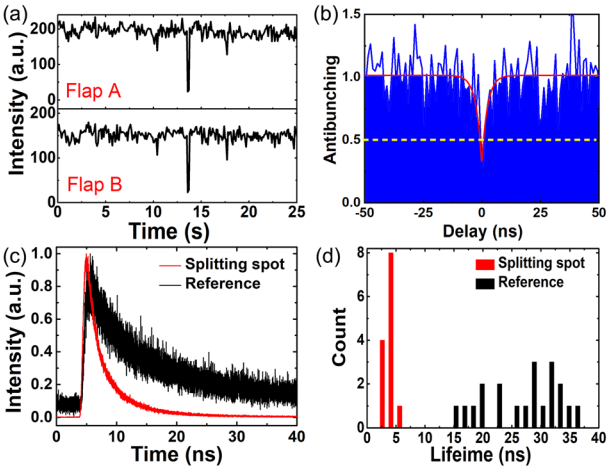

Figure 3: (a) Fluorescence intensity time traces of Flap A and Flap B in Figure 2b. (b) Autocorrelation curve of the photons emitted from the single quantum dot located above the silver nanowire. The red line is the fitting curve. (c) Decay curves of the photons emitted from the single quantum dot. The black and red lines denote the decay curves of the photons emitted from single quantum dots doped in PMMA on glass and located above a silver nanowire, respectively. (d) Statistics of the lifetimes of the single quantum dots doped in PMMA on glass (black squares) and located above a silver nanowire (red squares).

background fluorescence from the PMMA film is also measured (not shown here), and the lifetime is approximately $\tau_{PMMA} = 7.0$ ns, which is close to the fast lifetime ($\tau^{r}_{fast} = 6.8$ ns). Thus, we attribute the fast lifetime ($\tau^{r}_{fast} = 6.8$ ns) to the lifetime of the background fluorescence from the PMMA film, and the slow lifetime of $\tau^{r}_{slow} = 30.3$ ns is the lifetime of a single quantum dot. The red line in Figure 3c is the decay curve of the photons emitted from a single quantum dot located above a silver nanowire (Figure 2b). By fitting the red line with a double exponential function, the fast lifetime is found to be $\tau^{s}_{fast} = 2.2$ ns, and the slow lifetime is $\tau^{s}_{slow} = 7.3$ ns. In our experiment, the orientations of PMMA molecules are random, and the thickness of the PMMA film is 50 nm. Hence, the lifetime for most PMMA molecules are not affected. Hence, $\tau^{s}_{slow} = 7.3$ ns is the lifetime of the fluorescence from these unaffected PMMA molecules. According to the definition, [14] the Purcell factor is equal to $f_P = \overline{\tau^{r}}/\tau^{s}_{fast} \times f_P^{PMMA} = 25.4/2.2 \times 1.5 \approx 17.3$ when a single quantum dot is located above a silver nanowire. Here, $\overline{\tau^{r}} \approx 25.4$ ns is the average lifetime of single quantum dots doped in PMMA on a glass substrate (see Figure 3d), and $f_P^{PMMA} = 1.5$ is the calculated Purcell factor when the quantum dot is in PMMA [35]. This indicates that the spontaneous emission rate of the single quantum dot located above the silver nanowire is enhanced by 17.3 times. The lifetimes of single quantum dots in a number of samples are also measured, and the results are displayed in Figure 3d. The black squares denote the lifetimes of the single quantum dots doped in PMMA on a glass substrate (τ^{r}). The fluctuation of the lifetimes of these quantum dots on the glass substrate is attributed to the difference in the colloidal nanocrystal quantum dots synthesized in the chemical process [1, 19, 35]. The red squares in Figure 3d are the lifetimes of single quantum dots located above silver nanowires placed on a gold substrate (τ^{s}). From Figure 3d, it can be observed that the average lifetime ($\overline{\tau^{s}} \approx 3.2$ ns) of single quantum dots located above silver nanowires is much smaller than that ($\overline{\tau^{r}} \approx 25.4$ ns) of the single quantum dots doped in PMMA on a glass substrate. Due to the spin-coated method, the distance between a single quantum dot and a silver nanowire together with the orientation of CQDs is random, which will affected the Purcell factor. In order to eliminate the influence of the position and orientation of quantum dots, we use the lifetime of a specific quantum dot located on the silver nanowire to calculate the Purcell factor.

2.2 Simulation

To understand the underlying mechanism of the above pattern- and polarization-tailoring phenomena in the symmetric hybrid nanostructure, a numerical simulation is implemented (see Appendix C: Simulation), and the results are displayed in Figure 4. The quantum dots are associated with 2D dipole moments located in a plane and a missing dipole moment along the direction perpendicular to the plane [1–7]. In our experiment, the CQDs are spin-coated on the metal surface, and thus dipole moments are randomly oriented. Hence, the Purcell factors for the dipole oriented along the x-, y-, and z-axes in the hybrid system are all calculated. The Purcell factor, which is corresponding to the enhancement of spontaneous radiative rates, is defined as $F_p = \gamma_{total}/\gamma_0$ [14]. Herein, γ_{total} and γ_0 are the decay rate of the dipole in a structure and a vacuum, respectively. Based on the definition, a nonradiative decay channel could also give rise to the enhancement of spontaneous radiative rates [19]. For $d = 5$ nm, the calculated results of the Purcell factors for different silver nanowire radii are shown in Figure 4a. It is observed that the Purcell factors for the dipole oriented along the z-axis (blue line with $f_{Pz} \approx 20.0$) are much greater than those for the dipole oriented along the x- and y-axes (black line with $f_{Px} \approx 4$ and red line with $f_{Py} \approx 0.5$). The reason is that the electric vectors of the z-oriented dipole are mainly parallel to those of the SPPs on the silver surface [36, 37]. As a result, the dipole oriented along the z-axis is extracted in this hybrid system with $d = 5$ nm.

For R = 130 nm (the pink dashed line in Figure 4a), the Purcell factors for the dipole oriented along the x-, y-, and z-axes are calculated for different values of d (the distance between the dipole and the silver nanowire along the z-axis), and the results are shown in Figure 4b. When d increases, the Purcell factors of the z-oriented dipole (f_{Pz}) sharply decrease, as shown by the blue line in Figure 4b. The reason is that the photons emitted from the dipole are mainly coupled to the SPP modes only when the dipole is very close to the metallic nanostructures (several nanometers) [19], and SPPs can increase the emission rate of the dipole. Therefore, it is better to extract and largely enhance only the z-oriented dipole by choosing a small distance (d). For d = 5 nm, the Purcell factor ($f_{Pz} \approx 20.0$) is nearly equal to that in the experiment.

In addition, Figure 4a shows that the Purcell factors for the dipole oriented along the x-, y-, and z-axes slightly change with increasing radius of the silver nanowire,

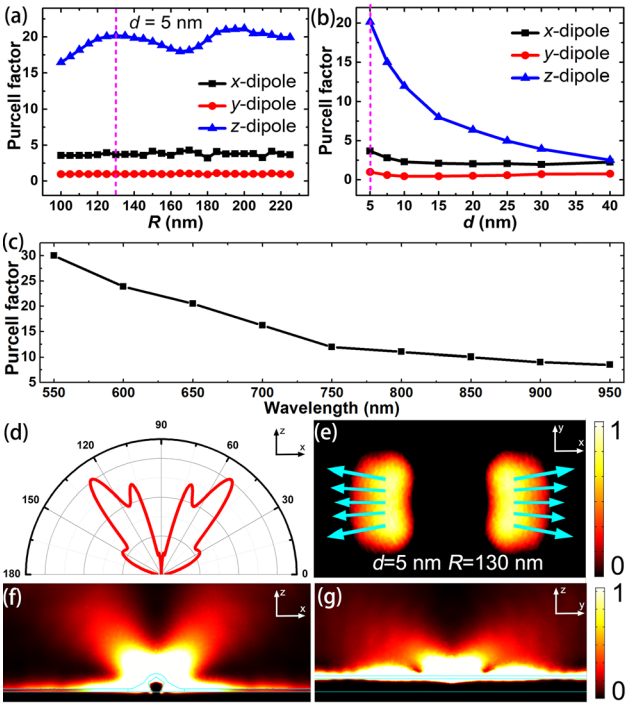

Figure 4: (a) Variation in the Purcell factor with the radius of the silver nanowire for the dipole oriented along the x-, y-, and z-axes when d = 5 nm. (b) Variation in the Purcell factor for the dipole oriented along the x-, y-, and z-axes with d (the distance between the dipole and the silver nanowire) when R = 130 nm. (c) Response spectrum of the Purcell factors for the proposed metallic nanostructure with d = 5 nm. (d) Far-field ($|E_{far}|^2$) distribution in different directions of the x-z plane with x = 0 μm and (e) intensity ($|E|^2$) distribution in the x-y plane with z = 2 μm when d = 5 nm and R = 130 nm. Distributions of the intensity ($|E|^2$) in (e) the x-z plane with y = 0 μm and (f) the y-z plane with x = 0 μm.

indicating that no strong resonances occur here. Hence, matching between the emission wavelength of the single quantum dot and the resonant wavelength of the metallic nanostructure is not required here, which is quite different from previous works using SPP resonant modes. The nonresonant enhancement here results from the interaction between the z-oriented dipole and the induced electron-hole pair in the silver nanowire [38]. The enhancement of spontaneous radiative rates (Purcell enhancement) increases dramatically (inversely proportional to the third power of the distance) when the distance between the z-oriented dipole and the induced electron-hole pair decreases, which agrees well with the results in Figure 4b. M. L. Brongersma's Group has also reported this strong nonresonant enhancement when a dipole is placed on a metal surface [39]. The response spectrum of the Purcell factors for the proposed hybrid structure is simulated (R = 130 nm and d = 5 nm), and the result is shown in Figure 4c. It is observed that there is no resonance in Figure 4c, further confirming our above analysis. Hence, our hybrid structure exhibits a nonresonant enhancement of the spontaneous emission rate. The decrease in the Purcell factors with increasing wavelength is attributed to two factors. One is that the long wavelengths are far from the bulk plasmon resonance wavelength of silver ($\lambda_{pl} \approx$ 400 nm) [39]. The other is that the optical mode volume increases rapidly with increasing wavelength, making λ^3/V decrease when wavelengths increase from 550 to 950 nm [40].

For the dipole oriented along the z-axis at a small distance (d = 5 nm and R = 130 nm), denoted by the pink dashed lines in Figure 4a and b, the far-field ($|E_{far}|^2$) distribution in different directions of the x-z plane with x = 0 μm and the intensity ($|E|^2$) distribution in the x-y plane with z = 2 μm are shown in Figure 4d and e. From Figure 4d and e, it is observed that the emission pattern of the z-oriented dipole is split into two distinct flaps, agreeing well with the experimental results (Figure 2a and b). The intensity ratio of the two splitting flaps, defined as the quotient between the intensity of the two flaps and the total emission intensity from the dipole, is calculated to be approximately η = 18%. Because of the Purcell enhancement, the number of collected single photons from the dipole located above the silver nanowire becomes approximately 5.5 times $[f_{Pz} \times n/(f_{Pz}^{glass} \times n^{glass}) = 20 \times 18\%/(2 \times 33\%) \approx 5.5]$ that from the dipole on a glass substrate under the same pump intensity. Here, the simulated Purcell factor and the collection efficiency (numerical aperture [NA] = 0.8) of the dipole on a glass substrate are $f_{Pz}^{glass} = 2$ and $\eta^{glass} = 33\%$ when the distance between the dipole and the glass substrate is 5 nm.

The cyan arrows in Figure 4e represent the electric vectors, indicating a central symmetry about the *z*-axis. The reason is that the electric vectors of the *z*-oriented dipole are centrally symmetric about the *z*-axis.

The intensity ($|E|^2$) distribution in the *x*-*z* plane with $y = 0$ μm for the hybrid system is also given in Figure 4f. It is also clearly observed that there are two radiation directions, which correspond to the two splitting flaps, as shown in Figure 4e. Figure 4g displays the intensity distribution ($|E|^2$) in the *y*-*z* plane with $x = 0$ μm for the hybrid system. It is observed that the photons emitted from the dipole are mainly coupled to the SPP waveguide mode supported by the silver nanowire and then propagate along the silver nanowire. Hence, the photons emitted from the dipole radiate to free space only in the direction perpendicular to the silver nanowire, and the two splitting flaps are on both sides of the silver nanowire, as shown in Figures 2b and 4e. When the dipole is not located above the top edge of the silver nanowire, the simulation shows that the intensities of the flaps on the opposite sides of the nanowires are not equal, which is also observed in the experiment. In addition, when the distance between a *z*-oriented dipole and gold substrate is fixed, the distributions of $|E|^2$ for different nanowire shapes (pentagon, circle, and rectangle) are also simulated. The simulation results show that the shape of the nanowire section has little impacts on the distributions of $|E|^2$.

2.3 Image dipole model

To give a direct physics picture of the hybrid system shown in Figure 1, we propose using simple image dipole theory [36] to explain the pattern-splitting phenomenon in the *x*-*z* plane with $y = 0$ μm. In the hybrid structure (Figure 1a and b), the silver nanowire is used to extract and enhance the dipole oriented along the *z*-axis when the dipole is close to the top edge of the nanowire (with *d* being several nanometers). Moreover, the silver nanowire is used to prop up the *z*-oriented dipole with a large separation (z > 200 nm) from the gold substrate. This large separation can avoid strong coupling of the dipole emission to the SPPs on the surface of the gold substrate. Hence, the gold substrate in the hybrid system acts only as a mirror. Based on this analysis, the symmetric hybrid structure is simplified to a *z*-oriented primary dipole (Q_1) located above the gold substrate with a large separation of z_0, as shown in Figure 5a. This is a 2D model that only considers the direction perpendicular to the silver nanowire. The image dipole (Q_2) with the same orientation and amplitude is at the mirror point of the primary dipole [36]. Therefore, the total intensity distribution above the metal surface is the interference pattern of the primary dipole and the image dipole. The interference pattern can be observed by in a microscope with an objective of NA = 0.8.

To test the simple model and the above analysis, both a simulation and theoretical equations are provided. Using COMSOL, the intensity ($|E|^2$) distribution of a *z*-oriented primary dipole located above a gold substrate with a separation of $z_0 = [1 + \sin(72°)]R + d = 261$ nm is simulated, as shown in Figure 5b. The intensity distribution is very similar to that in Figure 4f. In Figure 5c, the interference pattern of the *z*-oriented primary dipole and the image dipole with a separation of $2 \times z_0 = 522$ nm is calculated, and the intensity ($|E|^2$) distribution is similar to that in Figure 4f. The similarity of Figures 4f, 5b, and 5c strongly confirms the simple model in Figure 5a. Based on the Fraunhofer approximation, the interference pattern of the primary dipole and the image dipole in the polar coordinate system can be written as

$$I(\theta) \propto \sin^2\theta\left(2+\frac{2\cos(4\pi z_0\cos\theta)}{\lambda}\right), \quad \theta = \arctan\left(\frac{x}{z}\right), \quad (1)$$

The calculated results are displayed in Figure 5d, which is similar to Figure 4d, further confirming our simple model. The exact image dipole theory for the Sommerfeld half-space problem, which has been solved by Esko Alanen et al. [41] is more complicated. In addition, the separation between the dipole (Q_1) and the surface of the gold substrate is simplified to $z_0 = [1 + \sin(72°)]R + d$. The difference

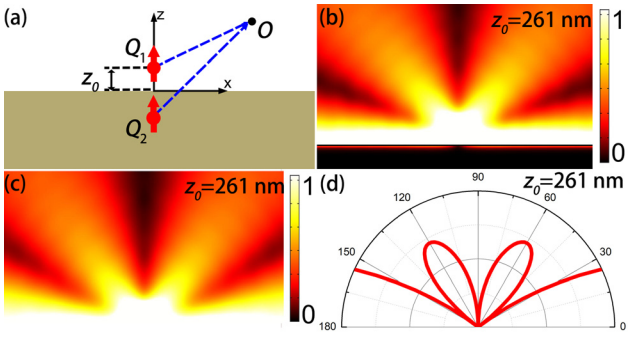

Figure 5: (a) Two-dimensional simplified image dipole model. A *z*-oriented primary dipole (Q_1) is placed above a gold substrate. The image dipole (Q_2) with the same orientation and magnitude is at the mirror point of the dipole. The separation between the dipole and the gold substrate is z_0. (b) Intensity ($|E|^2$) distribution of a *z*-oriented primary dipole located above a gold substrate ($z_0 = 261$ nm). (c) Intensity ($|E|^2$) distribution of the interference between the primary dipole and the image dipole ($z_0 = 261$ nm). (d) Polar plots of the interference pattern of the primary dipole and the image dipole in the polar coordinate system ($z_0 = 261$ nm).

in the far-field distributions in the direction along the metal surface in Figures 4d and 5d is attributed to the fact that the simple dipole model does not consider the influence of the silver nanowire and the metal loss. However, this 2D simplified image dipole model is sufficient to explain the pattern-splitting phenomenon in the experiment for the collection angle of the objective (NA = 0.8). In addition, a *z*-oriented dipole above a silver nanowire on a glass substrate is also simulated, and no interference patterns above the glass substrate are observed, further verifying the image dipole model.

2.4 Expanding the structural-symmetry-tailoring principle

The structural-symmetry-tailoring principle can be expanded to more complex structures with a higher-order symmetry axis, and more splitting flaps with a radial polarization state can be realized. Some examples are given in the following. When a *z*-oriented dipole is located directly above (d = 5 nm) the crossing point of Y-shaped silver nanowires placed on a gold substrate (Figure 6a), this hybrid system has a threefold symmetry axis, corresponding to the C_3 point group. The number of splitting flaps is three, as shown in Figure 6b. When a *z*-oriented dipole is located directly above the crossing point of two orthogonal silver nanowires on a gold substrate (Figure 6c), this hybrid system has a fourfold symmetry axis, corresponding to the C_4 point group. The number of splitting flaps is four, as shown in Figure 6d. When a *z*-oriented dipole is located directly above a spherical silver nanoparticle on a gold substrate (Figure 6e), this hybrid system has an infinite-fold symmetry axis, corresponding to the C_∞ point group. The number of splitting flaps is infinite. As a result, the infinite flaps form a doughnut-shaped pattern, as shown in Figure 6f. Moreover, the polarizations of these emitted photons are centrally symmetric about the symmetric axis of the metallic nanostructure. Thus, single-photon emission with a radial polarization state is predicted in Figure 6e and f. The above examples further verify the structural-symmetry-tailoring mechanism. In the proposed hybrid structure, it can be concluded that the number of flaps is equal to the order of the symmetric axis, and the electric vectors of the emitted photons are centrally symmetric about the symmetric axis of the metallic nanostructure.

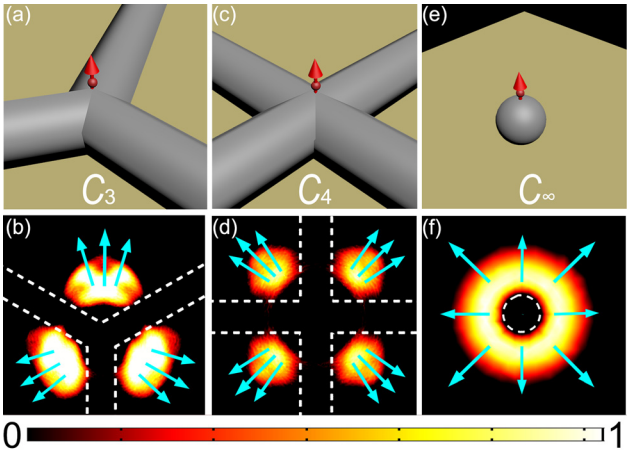

Figure 6: (a) Schematic diagram of Y-shaped silver nanowires on a gold substrate. A *z*-oriented dipole is located directly above (d = 5 nm) the crossing point of the Y-shaped silver nanowires. (b) Intensity ($|E|^2$) distribution in the *x*-*y* plane with z = 2 μm. The white dashed lines are the profile of the Y-shaped silver nanowires. (c) Schematic diagram of two orthogonal silver nanowires on a gold substrate. (d) Intensity ($|E|^2$) distribution in the *x*-*y* plane with z = 2 μm. The white dashed lines are the profiles of the two orthogonal silver nanowires. (e) Schematic diagram of a spherical silver nanoparticle on a gold substrate. (f) Intensity ($|E|^2$) distribution in the *x*-*y* plane with z = 2 μm. The white dashed lines are the profile of the spherical silver nanoparticle.

3 Discussion

In this study, the emission patterns and polarizations of a single quantum dot were tailored by the symmetry of the metallic nanostructure. Here, the nonresonant silver nanowire was used to both enhance the emission rate and extract the dipole oriented along the *z*-axis. Thus, matching between the emission wavelength of the single quantum dot and the resonant wavelength of the metallic nanostructure was no longer required. In the experiment, it was observed that the far-field emission pattern of the single quantum dot located close (approximately several nanometers) to the top edge of the nanowire was split into two flaps. The electric vectors of the emitted photons were centrally symmetric about the symmetric axis because of the symmetry of the hybrid nanostructure. The shape of the nanowire section has little influence on the pattern and polarization. The measured Purcell factor was 17.3. The pattern-splitting phenomenon was well explained by both the simulation and the image dipole model. Based on this structural-symmetry-tailoring mechanism, more splitting flaps with a radial polarization state of the single-photon emission were predicted by crossing the basic unit structures. The structural-symmetry-tailoring mechanism might open up new possibilities and degrees of freedom for designing multifunctional and novel quantum-plasmonic devices.

Acknowledgments: This work was supported by the National Basic Research Program of China (2017YFF0206103 and 2018YFA0704400), the National Natural Science Foundation of China (61922002, 91850103, 11674014, 61475005, 11527901, 11525414, and 11134001), and the Beijing Natural Science Foundation (Z180015).

Author contribution: Jianjun Chen proposed the idea. Jianjun Chen and Guorui Zhang conceived the experiment. Guorui Zhang carried out the sample fabrication, optical measurement, and simulation. Jianjun Chen and Guorui Zhang conceived the experiment, carried out the analysis, and wrote the main manuscript text. Ying Gu and Qihuang Gong gave help discussions. All the authors have accepted responsibility for the entire content of this submitted manuscript and approved submission.

Research funding: This work was supported by the National Basic Research Program of China (2017YFF0206103 and 2018YFA0704401), the National Natural Science Foundation of China (61922002, 91850103, 11674014, 61475005, 11527901, 11525414, and 11134001), and the Beijing Natural Science Foundation (Z180015).

Conflict of interest statement: The authors declare no conflicts of interest regarding this article.

Appendix A: Fabrication

Silver nanowires with radii ranging from 80 to 140 nm are first drop-coated on a gold substrate (thickness of 200 nm). The gold substrate is treated by oxygen plasma for 5 min at a power of P = 80 W. The density of the silver nanowires is approximately three nanowires per 200 μm^2. Then, a poly(methyl methacrylate) (PMMA) film doped with quantum dots (CdSe/ZnS) is spin-coated on the same gold substrate. The thickness of the PMMA film is approximately t = 50 nm. The central wavelength of the photons emitted from the quantum dots is approximately λ_{em} = 650 nm.

Appendix B: Measurement

In the homemade microscope, a continuous laser beam with λ_{ex1} = 405 nm is obliquely focused on the sample to excite the quantum dots. The incident angle of the laser is approximately 60 degrees. The power of the laser is 2.6 mW, and the spot size is approximately 120 × 60 μm. After passing through a longpass filter of λ_{cut} = 600 nm, the photons emitted from the quantum dots are collected by an objective (NA = 0.8). Then, the collected photons are imaged on a scientific complementary metal oxide semiconductor (sCMOS) camera.

In the TCSPC measurement system, a pulse laser beam (central wavelength of λ_{ex2} = 518 nm and repetition frequency of 10 MHz) is focused on the sample by an objective (NA = 0.8) to excite an individual quantum dot. The photons emitted from the quantum dot are collected by the same objective.

Appendix C: Simulation

The simulation is carried out by using COMSOL Multiphysics software. In the basic unit structure (Figure 1a), the permittivities of silver and gold are taken from Ref. [42]. The structure is covered by a PMMA film (refractive index of $n = \varepsilon^{1/2} = 1.5$ and thickness of t = 50 nm). The quantum dot is simulated as a dipole, [14, 43] and it is located at the top edge of the silver nanowire, as shown in Figure 1b. The emission wavelength of the dipole is set to λ_{em} = 650 nm. The position of the dipole is (0,0, [1 + sin(72°)] $R + d$).

References

[1] I. Aharonovich, D. Englund, and M. Toth, "Solid-state single-photon emitters," *Nat. Photonics*, vol. 10, pp. 631–641, 2016.
[2] S. A. Empedocles, R. Neuhauser, and M. G. Bawendi, "Three-dimensional orientation measurements of symmetric singlechromophores using polarizationmicroscopy," *Nature*, vol. 399, pp. 126–130, 1999.
[3] S. Jaetae, F. Rafal, K. Wan-Joong, et al., "Hybrid optical materials of plasmon-coupled CdSe/ZnS coreshells for photonic applications," *Opt. Mater. Express*, vol. 2, p. 1026, 2012.
[4] F. Kaiser, V. Jacques, A. Batalov, P. Siyushev, F. Jelezko, and J. Wrachtrup, "Polarization properties of single photons emitted by nitrogen-vacancy defect in diamond at low temperature," *ArXiv*, vol. 0906, p. 3426, 2009.
[5] P. Zhao, M. Amani, D. H. Lien, et al., "Measuring the edge recombination velocity of monolayer semiconductors," *Nano Lett.*, vol. 17, pp. 5356–5360, 2017.
[6] X. Li, G. D. Shepard, A. Cupo, et al., "Nonmagnetic quantum emitters in boron nitride with ultranarrow and sideband-free emission spectra," *ACS Nano.*, vol. 11, pp. 6652–6660, 2017.
[7] T. T. Tran, K. Bray, M. J. Ford, M. Toth, and I. Aharonovich, "Quantum emission from hexagonal boron nitride monolayers," *Nat. Nanotechnol.*, vol. 11, pp. 37–41, 2016.
[8] S. K. H. Andersen, S. Kumar, and S. I. Bozhevolnyi, "Ultrabright linearly polarized photon generation from a nitrogen vacancy center in a nanocube dimer antenna," *Nano Lett.*, vol. 17, pp. 3889–3895, 2017.
[9] T. B. Hoang, G. M. Akselrod, and M. H. Mikkelsen, "Ultrafast room-temperature single photon emission from quantum dots coupled to plasmonic nanocavities," *Nano Lett.*, vol. 16, pp. 270–275, 2016.
[10] T. B. Hoang, G. M. Akselrod, C. Argyropoulos, J. Huang, D. R. Smith, and M. H. Mikkelsen, "Ultrafast spontaneous emission

source using plasmonic nanoantennas," *Nat. Commun.*, vol. 6, p. 7788, 2015.
[11] S. I. Bogdanov, M. Y. Shalaginov, A. S. Lagutchev, et al., "Ultrabright room-temperature sub-nanosecond emission from single nitrogen-vacancy centers coupled to nanopatch antennas," *Nano Lett.*, vol. 18, pp. 4837–4844, 2018.
[12] F. Werschler, B. Lindner, C. Hinz, et al., "Efficient emission enhancement of single CdSe/CdS/PMMA quantum dots through controlled near-field coupling to plasmonic Bullseye resonators," *Nano Lett.*, vol. 18, pp. 5396–5400, 2018.
[13] X. Duan, J. Ren, F. Zhang, et al., "Large Purcell enhancement with efficient one-dimensional collection via coupled nanowire-nanorod system," *Nanotechnology*, vol. 29, p. 045203, 2018.
[14] H. Lian, Y. Gu, J. Ren, F. Zhang, L. Wang, and Q. Gong, "Efficient single photon emission and collection based on excitation of gap surface plasmons," *Phys. Rev. Lett.*, vol. 114, p. 193002, 2015.
[15] X. Chen, Y. H. Chen, J. Qin, et al., "Mode modification of plasmonic gap resonances induced by strong coupling with molecular excitons," *Nano Lett.*, vol. 17, pp. 3246–3251, 2017.
[16] F. Prins, D. K. Kim, J. Cui, et al., "Direct patterning of colloidal quantum-dot thin films for enhanced and spectrally selective out-coupling of emission," *Nano Lett.*, vol. 17, pp. 1319–1325, 2017.
[17] S. Morozov, M. Gaio, S. A. Maier, and R. Sapienza, "Metal-dielectric parabolic antenna for directing single photons," *Nano Lett.*, vol. 18, pp. 3060–3065, 2018.
[18] A. G. Curto, G. Volpe, T. H. Taminiau, M. P. Kreuzer, R. Quidant, and N. F. van Hulst, "Unidirectional emission of a quantum dot coupled to a nanoantenna," *Science*, vol. 329, pp. 930–933, 2010.
[19] A. V. Akimov, A. Mukherjee, C. L. Yu, et al., "Generation of single optical plasmons in metallic nanowires coupled to quantum dots," *Nature*, vol. 450, pp. 402–406, 2007.
[20] G. Lu, T. Zhang, W. Li, L. Hou, J. Liu, and Q. Gong, "Single-molecule spontaneous emission in the vicinity of an individual gold nanorod," *J. Phys. Chem. C.*, vol. 115, pp. 15822–15828, 2011.
[21] P. Senellart, G. Solomon, and A. White, "High-performance semiconductor quantum-dot single-photon sources," *Nat. Nanotechnol.*, vol. 12, pp. 1026–1039, 2017.
[22] V. Parigi, V. D'Ambrosio, C. Arnold, L. Marrucci, F. Sciarrino, and J. Laurat, "Storage and retrieval of vector beams of light in a multiple-degree-of-freedom quantum memory," *Nat. Commun.*, vol. 6, p. 7706, 2015.
[23] A. Nicolas, L. Veissier, L. Giner, E. Giacobino, D. Maxein, and J. Laurat, "A quantum memory for orbital angular momentum photonic qubits," *Nat. Photonics*, vol. 8, pp. 234–238, 2014.
[24] B. Ndagano, B. Perez-Garcia, F. S. Roux, et al., "Characterizing quantum channels with non-separable states of classical light," *Nat. Phys.*, vol. 13, pp. 397–402, 2017.
[25] C. Gabriel, A. Aiello, W. Zhong, et al., "Entangling different degrees of freedom by quadrature squeezing cylindrically polarized modes," *Phys. Rev. Lett.*, vol. 106, p. 060502, 2011.
[26] V. Giovannetti, S. Lloyd, and L. Maccone, "Quantum enhanced positioning and clock synchronization," *Nature*, vol. 412, p. 417, 2001.
[27] G. Brida, M. Genovese, and I. Ruo Berchera, "Experimental realization of sub-shot-noise quantum imaging," *Nat. Photonics*, vol. 4, pp. 227–230, 2010.
[28] V. Boyer, A. M. Marino, R. C. Pooser, and P. D. Lett, "Entangled images from four-wave mixing," *Science*, vol. 321, pp. 544–547, 2008.
[29] K. Rong, F. Gan, K. Shi, S. Chu, and J. Chen, "Configurable integration of on-chip quantum dot lasers and subwavelength plasmonic waveguides," *Adv. Mater.*, vol. 30, p. 1870148, 2018.
[30] Q. Li, H. Wei and H. Xu, "Resolving single plasmons generated by multiquantum-emitters on a silver nanowire," *Nano Lett.*, vol. 14, pp. 3358–3363, 2014.
[31] Q. Li, H. Wei and H. Xu, "Quantum yield of single surface plasmons generated by a quantum dot coupled with a silver nanowire," *Nano Lett.*, vol. 15, pp. 8181–8187, 2015.
[32] L. Su, G. Lu, B. Kenens, et al., "Visualization of molecular fluorescence point spread functions via remote excitation switching fluorescence microscopy," *Nat. Commun.*, vol. 6, p. 6287, 2015.
[33] C. Gruber, A. Trugler, A. Hohenau, U. Hohenester, and J. R. Krenn, "Spectral modifications and polarization dependent coupling in tailored assemblies of quantum dots and plasmonic nanowires," *Nano Lett.*, vol. 13, pp. 4257–4262, 2013.
[34] H. Takata, H. Naiki, L. Wang, et al., "Detailed observation of multiphoton emission enhancement from a single colloidal quantum dot using a silver-coated AFM tip," *Nano Lett.*, vol. 16, pp. 5770–5778, 2019.
[35] M. Zhu, J. Zhou, Z. Hu, H. Qin, and X. Peng, "Effects of local dielectric environment on single-molecule spectroscopy of a CdSe/CdS core/shell quantum dot," *ACS Photonics*, vol. 5, pp. 4139–4146, 2018.
[36] L. Novotny and B. Hecht, "Dipole emission near planar interfaces," in *Principles of Nano-OpticsThe Edinburgh Building, Cambridge CB2 8RU*, 2nd ed. The Edinburgh Building, Cambridge CB2 8RU, UK, Cambridge University Press, 2013, pp. 313–337.
[37] W. L. Barnes, A. Dereux, and T. W. Ebbesen, "Surface plasmon subwavelength optics," *Nature*, vol. 424, p. 824, 2003.
[38] Y. Chen, T. R. Nielsen, N. Gregersen, and J. J. P. R. B. Mørk, "Finite-element modeling of spontaneous emission of a quantum emitter at nanoscale proximity to plasmonic waveguides," *Phys. Rev. B.*, vol. 81, p. 125431, 2010.
[39] Y. C. Jun, R. D. Kekatpure, J. S. White, and M. L. Brongersma, "Nonresonant enhancement of spontaneous emission in metal-dielectric-metal plasmon waveguide structures," *Phys. Rev. B.*, vol. 78, p. 153111, 2008.
[40] C. Sun, K. Rong, Y. Wang, H. Li, Q. Gong, and J. Chen, "Plasmonic ridge waveguides with deep-subwavelength outside-field confinements," *Nanotechnol.*, vol. 27, p. 065501, 2016.
[41] I. V. Lindell and E. Alanen, "Exact image theory for the Sommerfeld half-space problem, Part I: vertical magnetic dipole," *IEEE Transactions on Ant. & Propag.*, vol. 32, pp. 1027–1032, 2003.
[42] P. B. Johnson and R. W. Christy, "Optical constants of the noble metals," *Phys. Rev. B.*, vol. 6, pp. 4370–4379, 1972.
[43] H. Siampour, S. Kumar, and S. I. Bozhevolnyi, "Nanofabrication of plasmonic circuits containing single photon sources," *ACS Photonics*, vol. 4, pp. 1879–1884, 2017.